Oct 23rd, 12:00 AM

A Comparison of Finite Element Nonlinear Analyses with Tests of Stressed Arch Frames

Murray J. Clarke

Gregory J. Hancock

Tenth International Specialty Conference on Cold-formed Steel Structures
St. Louis, Missouri, U.S.A., October 23-24, 1990

A COMPARISON OF FINITE ELEMENT NONLINEAR ANALYSES WITH TESTS OF STRESSED ARCH FRAMES

Murray J. Clarke[1] and Gregory J. Hancock[2]

Summary

The paper describes a nonlinear analysis which can be applied to study the strength and behaviour of stressed arch (STRARCH) frames. The unique feature of the structural system is the way the arches are erected without the use of cranes or scaffolding but by the use of a post-tensioning process. For some highly curved structures, the top chord may be plastically deformed during the erection procedure.

The finite element nonlinear analysis has been developed to simulate the geometric nonlinear behaviour and plasticity in the stressed arch, particularly the top chord. The paper describes the nonlinear analysis including the arch elements used, the implementation of plasticity and the iterative strategies employed to solve the nonlinear problem, particularly in the post-ultimate range where snap-through may occur.

A series of tests on panels removed from the stressed arch frames, which have been described in earlier papers and reports, are simulated using the nonlinear analysis to verify its accuracy for application to stressed arch frames. A brief description of the application of the nonlinear analysis and panel tests to complete systems is also provided in the paper.

1 Postgraduate Student, School of Civil and Mining Engineering, University of Sydney, Australia, 2006.

2 Associate Professor, School of Civil and Mining Engineering, University of Sydney, Australia, 2006.

1 INTRODUCTION

The stressed arch structural system concept is a recent development in steel structures by Strarch International Limited of Melbourne, Australia. The structural system comprises prefabricated truss frames composed of Australian produced cold-formed hollow sections, which are erected by a post-tensioning stressing procedure and results in curving of the top chord into its final configuration (Engineering News-Record 1988). The structural system is claimed to offer substantial economic advantages in fabrication and erection compared to conventional truss structures and clear spans up to 94 m (308 ft) have been achieved successfully.

A detailed experimental research program has been performed at the University of Sydney to determine the strength of the top chord using frame sub-assemblages of the stressed arch system (University of Sydney 1987a, 1987b, 1989). The experimental program consisted of two series of experiments which are termed Series I and Series II here. The 11 specimens tested in Series I are denoted Panels SP1–SP11 and the results of this investigation have been published previously (Hancock, Key & Olsen 1988). The Series II specimens are labelled Panels SP12–SP15 and have been summarised previously with the Series I results in Hancock et al. (1989). The detailed behaviour of the Series II test specimens is presented in this paper, although the main purpose of the current work is to describe the nonlinear elasto-plastic finite element analysis which has been developed and the modelling employed to simulate the geometric nonlinear behaviour and plasticity in the stressed arch, particularly the top chord. The nonlinear analysis is used in this paper to simulate the behaviour of the Series II panel tests. More detailed information on the experimental procedures and results and the finite element simulations than is provided in this paper is given in the companion report by Clarke & Hancock (1989).

The paper describes the nonlinear analysis including the arch elements used, the implementation of plasticity and the iteration strategies employed to solve the nonlinear problem, especially in the post-ultimate regime where snap-through may occur. The results of tension coupon tests, compression coupon tests and residual stress measurements performed on a representative top chord section are reported. The ultimate strengths and load versus deflection behaviour for Panels SP12–SP15 show excellent agreement with the experimental results and justify the rigorous approach to both the experimental and theoretical aspects of the investigation.

2 NONLINEAR FINITE ELEMENT ANALYSIS

2.1 The Isoparametric Curved Beam Element

2.1.1 Element Geometry

The finite element described in this paper is two-noded, curved and isoparametric and is suited to the in-plane analysis of arches as well as beam-columns and rigidly con-

nected plane frame structures. The element formulation is essentially a one-dimensional implementation of the axisymmetric shell element employed successfully by Teng & Rotter (1989).

The geometry of the element is shown in Fig. 1. The element nodal coordinates are defined in a global rectangular cartesian axis system by (x, y) coordinates. The slope of the element at the nodes is defined by the rate of change of the x and y coordinates with respect to arc-length s, given by dx/ds and dy/ds respectively. In addition, the curvature of the element at the nodes, and the rate of change of curvature at the nodes with respect to arc-length are defined by $d\phi/ds$ and $d^2\phi/ds^2$ respectively. The geometry within the element is interpolated from the nodal values using cubic Hermitian polynomial interpolating functions. The element description enables the initial structure geometry, including geometric imperfections of arbitrary shape, to be precisely defined by the parameters x, y, ϕ, $d\phi/ds$ and $d^2\phi/ds^2$.

2.1.2 Element Displacements

The element *local* displacements in the curvilinear coordinate system consist of the local tangential displacement $\bar{u}$ and the local normal displacment $\bar{v}$ (Fig. 1). For a curved element, simple polynomial displacement fields defined in terms of the local displacements may produce spurious straining when the element undergoes rigid-body translation (Cook 1981), although convergence towards strain-free rigid body motion occurs as the angle subtended by each element decreases to zero.

To overcome the problem of spurious straining due to rigid body translation, element displacements are defined here in terms of the global rectangular cartesian coordinate system. Such a definition also allows compatibility and equilibrium requirements at complex junctions of elements to be achieved simply. The vector of element nodal displacements in global coordinates is defined as

$$\{d_e\} = \left\{ u_1 \quad \left(\frac{du}{ds}\right)_1 \quad v_1 \quad \left(\frac{dv}{ds}\right)_1 \quad u_2 \quad \left(\frac{du}{ds}\right)_2 \quad v_2 \quad \left(\frac{dv}{ds}\right)_2 \right\}^T \tag{1}$$

The global displacements u, v at any point in the element are interpolated from the element nodal displacements $\{d_e\}$ using the Hermitian cubic shape functions, in a similar manner to the element geometry.

2.2 Strain-Displacement Relations

For the in-plane analysis of frames, the state of strain is defined by one component of membrane strain, ϵ_s, along the element reference line, and one component of bending curvature, κ_s. The generalised strain vectors for strains arising from displacements $\{\varepsilon\}$ and strains arising from initial strains $\{\varepsilon_o\}$ are given by

$$\{\varepsilon\} = \{\epsilon_s \quad \kappa_s\}^T \tag{2}$$

and

$$\{\varepsilon_o\} = \{\epsilon_{so} \quad \kappa_{so}\}^T \tag{3}$$

The membrane strain and curvature of the beam reference line are given in a total Lagrangian formulation by

$$\epsilon_s = \beta_1 + \frac{1}{2}\left({\beta_1}^2 + {\beta_2}^2\right) \tag{4}$$

$$\kappa_s = -\frac{\partial \beta_2}{\partial s} \tag{5}$$

in which

$$\beta_1 = \frac{\partial \bar{u}}{\partial s} + \bar{v}\frac{\partial \phi}{\partial s} \tag{6}$$

$$\beta_2 = \frac{\partial \bar{v}}{\partial s} - \bar{u}\frac{\partial \phi}{\partial s} \tag{7}$$

The term β_2 represents the in-plane rotation. The strain-displacement relations defined above are valid for large displacements and moderate rotations and are a simplification of those derived by Rotter & Jumikis (1988) for the finite element analysis of axisymmetric thin shells.

2.3 Constitutive Relations

2.3.1 Stress-Strain Relations at a Point

In the present work only longitudinal strains are considered and so at any point in the cross-section, yielding is assumed to occur as a result of longitudinal stress only. In addition, the material stress-strain curve is assumed to be identical in tension and compression and the subsequent yield surface is defined by the isotropic hardening rule (Mendelson 1968; Armen 1979). The assumption of isotropic hardening is satisfactory provided the loading regime is static and does not lead to substantial elastic unloading. An incremental or flow theory of plasticity (Mendelson 1968) has been adopted here.

Up to the point of yield, or during elastic unloading from the yield surface, the strain increments are entirely elastic and the stress increments $d\sigma_s$ are computed simply as

$$d\sigma_s = E d\epsilon_s^z \tag{8}$$

in which E is Young's modulus and $d\epsilon_s^z$ is the strain increment at a level z above the element reference line. If the point is currently undergoing plastic straining, then the incremental stress-strain relation can be expressed

$$d\sigma_s = E_t d\epsilon_s^z \tag{9}$$

in which E_t is the tangent modulus of the uniaxial stress-strain curve, computed as a function of the current stress level or the equivalent plastic strain.

2.3.2 Generalised Stress Resultants and the Tangent Modulus Matrix

The vector of generalised stress resultants in the curved beam element is defined as

$$\{S\} = \{N_s \;\; M_s\}^T \tag{10}$$

in which N_s is the membrane stress resultant of axial force and M_s is the bending stress resultant of bending moment.

In an incremental elasto-plastic analysis, it is only possible to relate increments of generalised strain to increments of generalised stress. This is achieved via the tangent modulus matrix $[D_T]$ as

$$d\{S\} = [D_T]\, d(\{\varepsilon\} - \{\varepsilon_o\}) \tag{11}$$

in which

$$[D_T] \;=\; \begin{bmatrix} \int_A E_t\, dA & \int_A E_t z\, dA \\ \int_A E_t z\, dA & \int_A E_t z^2\, dA \end{bmatrix} \tag{12}$$

In Eqn 12, z is the coordinate in the cross-section above the element reference line and E_t is the elasto-plastic tangent modulus defined as a function of the stress or equivalent plastic strain at the considered point.

The integration of $[D_T]$ over the area of the cross-section is achieved by discretising the cross-section into a grid of monitoring points and applying Simpson's rule in two dimensions. Simpson's rule has superior accuracy than Gaussian quadrature for discontinuous functions. The stress resultants are also computed using Simpson's rule using the same monitoring point grid.

2.4 Nonlinear Total Equilibrium Equations

In a total Lagrangian formulation of the finite element method, the structure geometry, displacements, strains and stresses are referred to the initial or undeformed configuration. The principle of virtual displacements, which is applicable irrespective of the constitutive relations, can be used to formulate the element static total equilibrium equations in terms of the element displacements.

The principle of virtual displacements can be expressed as

$$\int_V d\epsilon\; \sigma\; dV = \pi \tag{13}$$

in which $d\epsilon$ is the variation in the Green's strain tensor arising from the virtual displacement field du, and σ is the Poila-Kirchoff stress tensor. As a consequence of the path-dependent nature of plasticity, the current stress state at any point in the element cannot be uniquely defined as a function of the total strain. The term π represents the virtual work performed in moving the external load system consisting of body forces q and surface tractions p through the virtual displacement field du and is defined by

$$\pi = \int_V du\, \rho q\, dV + \int_A du\, p\, dA \tag{14}$$

In Eqn 14, ρ is the mass density of the body and dV and dA are elemental volume and surface area respectively, all with reference to the undisplaced state.

The virtual work equation (Eqn 13) is nonlinear in the element nodal displacements and so cannot be solved directly. One approach to facilitate solution is to derive an incremental equation of equilibrium and set up an iterative technique to solve it.

2.5 Solving the Nonlinear Equilibrium Equations

The solution procedure for the total equilibrium equations requires a relationship between the increments of applied load and the resultant incremental displacements, valid for the current deformed configuration and material properties of the structure. The incremental equilibrium equations are furnished by taking a variation of the virtual work equation. The result can be expressed in the form

$$d\{\phi\} = [k_T]\, d\{d_e\} \tag{15}$$

in which $[k_T]$ is the tangent stiffness matrix for an element and relates the increment of nodal load $d\{\phi\}$ to the incremental nodal displacement $d\{d_e\}$. Elemental integrations are performed numerically using three point Gaussian quadrature to obtain maximum efficiency from a minimum number of monitoring stations along the element.

Before assembly of the global equation system, the nodal variables are transformed and the element stiffness matrix and load vector condensed using techniques similar to those described by Cook (1981). The transformation and condensation procedure constrains only the two translations and the in-plane rotation to be connected between adjacent elements meeting at a common node. Since the element stiffness matrix is formulated in a global axis system, a coordinate transformation from local to global coordinates is not required before assembly of the tangent stiffness matrix at the structure level.

The incremental-iterative solution technique used to solve the nonlinear equations uses either a conventional Newton-Raphson procedure, or a modified Newton-Raphson procedure (Zienkiewicz 1977) in conjunction with various iterative strategies that permit the load parameter to vary during equilibrium iterations. Such iterative strategies include the arc-length control method (Riks 1979; Crisfield 1981) and the displacement control method (Powell & Simons 1981). A comprehensive review and assessment of these iterative strategies has been undertaken by Clarke & Hancock (1988).

The panel tests discussed in this paper involved non-proportional loading and a degree of elastic unloading of the top chord from the yield surface. Consequently, the best results were obtained in the present investigation by employing the conventional Newton-Raphson method under constant load control. The load limit point was traversed by switching the iterative strategy to the modified Newton-Raphson based displacement control (Powell & Simons 1981) just prior to ultimate load. The controlled displacement component in this instance was the lateral deflection v_2 at the centre of the failing segment of the test panel (see Fig. 10 later), which was monotonically increasing throughout the entire loading regime.

In the iterative process, iterations on the material and geometric nonlinearities occur simultaneously. An accurate material state determination algorithm was employed to ensure that increments in stress are correctly deduced from increments in strain. The assumption of incremental reversibility proposed by Nyssen (1981), was employed to eliminate the path dependent nature of material state determination and to ensure that the correct stress-strain path was followed within a single iteration, thereby avoiding spurious numerical elastic unloading.

As a consequence of the path dependent nature of the flow rules of plasticity, the current stress, current yield stress and the current level of equivalent plastic strain are stored at each monitoring point and updated incrementally during the analysis.

3 EXPERIMENTAL INVESTIGATION

3.1 Overview of Experimental Program

The test panel geometries and top chord sections described in this paper were half the scale of those considered for use in a 94 m (308 ft) span STRARCH aircraft hanger. The four test panels are identified as Panels SP12–SP15 (University of Sydney 1989; Hancock et al. 1989).

The aim of the experimental program was to investigate the variation of both the top chord strength and the interaction between two adjacent segments of top chord, after each was subjected to different levels of initial curvature applied by means of the bottom chord and web members. The four Panels SP12–SP15 were tested to collapse. Subsequent residual stress measurements, tension and compression coupon tests, stub column tests and joint flexibility tests were performed to complete the test program and provide adequate data for subsequent theoretical analyses.

3.2 Top Chord Section and Material Properties

3.2.1 Top Chord Section Properties

The top chord of Panels SP12–SP14 consisted of a $102 \times 102 \times 4.9$ mm ($4.0 \times 4.0 \times 0.193$ in.) square hollow section (henceforth denoted 102 SHS) and the top chord of Panel SP15 was a $76 \times 76 \times 4.9$ mm ($3.0 \times 3.0 \times 0.193$ in.) square hollow section (henceforth denoted 76 SHS). Both top chord sections were of nominal strength Grade 350 ($F_Y = 350$ MPa (51 ksi)) according to AS1163 (Standards Association of Australia 1981). Average measured values of overall depth, overall width and plate thickness indicated that the actual values of area and second moment of area were less than the nominal values by approximately 2–3 %, with the major cause of the discrepancy being in the plate thickness. Consequently, the average measured plate thicknesses of 4.76 mm (0.187 in.) for the 76 SHS and 4.75 mm (0.187 in.) for the 102 SHS were used in preference to the nominal value of 4.9 mm (0.193 in.) in the

cross-section model of the top chord for the finite element simulations described in a later section of the paper.

3.2.2 Residual Stress Measurements

In the present investigation, only longitudinal residual stress was measured, since it is this component of the residual stress that is the most deleterious to column strength. Residual strain measurements were performed by taking readings on strain gauges on the inner and outer surfaces of a 102 SHS section at 7 locations around the perimeter before and after slicing longitudinal strips from the perimeter at the gauge locations shown in Fig. 2. The measurements were concentrated on one face (strain gauge numbers 1–10) although additional measurements at the centre of the two adjacent faces (strain gauges 11–14) were performed to provide some measure of the consistency of the results. The residual strains were found to be generally tensile on the outer surface and compressive on the inner surface which is in agreement with the findings of other researchers including Kato (1982), Beck & Lay (1973) and Key, Hasan & Hancock (1988). The residual strain distribution across the face was also fairly uniform.

The released surface strains may be considered to be composed of membrane and bending components. The membrane longitudinal residual stress and the bending longitudinal residual stress, calculated assuming $E = 205,000\,\text{MPa}$ (29,700 ksi), are shown together with the respective analytical models in a later section of the paper in Fig. 7. It is observed that the membrane residual stress distribution is quite low and exhibits a rapid variation across the face, being most compressive (average 60 MPa (8.7 ksi)) near the corners and assuming a value near zero for the central portion of the face. The experimental membrane distribution depicted in Fig. 7(c) does not satisfy axial equilibrium and consequently needed modification for incorporation in a residual stress analytical model as shown by the solid line in Fig. 7(c). The experimental bending stress distribution shown in Fig. 7(d) is quite uniform across the face with a mean value of approximately 225 MPa (32.6 ksi) (positive tensile on the outer surface) which is in excess of half the yield stress. Parametric studies by Davison & Birkemoe (1983) and Key & Hancock (1988) have shown that the through-thickness bending residual stress is the dominant cross-sectional parameter affecting the maximum strength of columns, primarily because of the early initiation of yielding on the inside of the faces and the subsequent lowering of flexural strength.

3.2.3 Material Properties

To ascertain the material properties of the cold-formed sections, tension coupons, compression coupons and combined tension-compression coupons were tested. All the coupons were cut from the 102 SHS used as the top chord in Panels SP12–SP14. The tension-compression coupon tests involved the following three stage process:

1. The coupons were originally made as tension coupons and tested in tension to a strain of 0.005. The coupons were then unloaded to zero stress.

2. The coupons were modified for testing in compression by removing the ends of the coupons used for gripping in the tension grips of the testing machine.

3. The modified coupons were then loaded in compression as far as was practically possible, with lateral restraint provided by a special compression testing device of the type described by Karren (1967).

The complexities of the cold-forming process invariably result in a variation of the fundamental material properties through the thickness of the plate. Consequently, the tension and compression coupon test results considered here can only reflect the average material behaviour through the thickness of the coupon. The presence of a high through-thickness residual stress gradient serves to further complicate the observed material behaviour.

An important characteristic exhibited by all the tension and compression coupons was the rounded nature of the stress-strain curve. Figure 3 shows the mean experimental results for the tension coupons and it is observed that there was no distinct yield plateau and transition to strain hardening as is typical of mild steel. Consequently, various values of proof stress have been reported here to characterise the stress-strain behaviour. The 0.2 % proof stress ($\sigma_{0.2}$) is often taken to be representative of the yield stress. The average results of the coupon tests are given in Table 1, in which σ_u is the ultimate tensile strength and e_{un} is the percentage of uniform elongation to ultimate. It is evident that the coupons from corner zones exhibited enhanced strength but degraded ductility compared with coupons from flat portions of the cross-section. The 0.2 % proof stress for corner tension coupons exceeded the 0.2 % proof stress for flat tension coupons by an amount greater than 30 %. Based on strain gauge readings, a Young's modulus equal to 205,000 MPa (29,700 ksi) has been adopted for calculation purposes in this paper.

Prior to testing, the coupons displayed a pronounced longitudinal curvature which arose from the release of the locked in bending residual stress. The action of clamping the tension coupons in the testing machine grips effectively straightened the coupons and reintroduced the bending residual stress distribution. The through-thickness bending residual stress distribution which therefore existed prior to tensioning is believed to cause substantial rounding of the observed stress-strain behaviour of the coupons. This assertion is supported by a numerical study of the curved tension coupons using the nonlinear finite element analysis. The rounded stress-strain curves derived from the tests and shown in Fig. 3 are therefore not simply a function of fundamental material behaviour, but are partially caused by the presence of the high through-thickness stress gradient which existed prior to tensioning and therefore initiated early yielding of portions of the tension coupons.

3.2.4 Stub Column Tests

Stub column tests were performed on both the 76 SHS and 102 SHS sections. The ultimate loads (P_{Su}) of the 76 SHS and 102 SHS sections were 641.0 kN (144.0 kips) and 733.0 kN (164.7 kips) respectively.

3.2.5 Web to Top Chord Joint Stiffness Tests

A series of tests on the web to top chord connection were performed as described in detail in Clarke & Hancock (1989) to determine the joint stiffness to in-plane rotation. On the evidence of tests on four different web to top chord joints, the mean joint rotational stiffness and standard deviation was determined as

$$k_\theta = \frac{M}{\theta} = (12.5 \times 10^6) \pm (1.1 \times 10^6)\,\text{Nmm} = 9.22 \pm 0.81\,\text{kip ft} \quad (16)$$

in which M is the moment acting at the joint and θ is the joint rotation. It is believed that the major source of variation in the joint stiffness was due to non-uniform welding between different joints. It was observed that those joints with heavier welding displayed a greater joint stiffness.

3.3 The Panel Tests

3.3.1 General

The test panels described in this paper are of the geometry shown in Fig. 4 and are denoted Panels SP12–SP15. The top chord of Panels SP12–SP14 consisted of $102 \times 102 \times 4.9$ mm ($4.0 \times 4.0 \times 0.193$ in.) SHS and the top chord of Panel SP15 consisted of $76 \times 76 \times 4.9$ mm ($3.0 \times 3.0 \times 0.193$ in.) SHS. The web members of all the test panels consisted of 48 mm (1.89 in.) external diameter by 3.2 mm (0.126 in.) thick circular hollow sections (CHS), flattened at the ends to facilitate welding to the top and bottom chords. The bottom chord of each test panel consisted of a $76 \times 76 \times 3.2$ mm ($3.0 \times 3.0 \times 0.126$ in.) SHS which was strain gauged and calibrated for use as a load cell. The top chord of each frame tested was located concentrically between the loading platens of the pinned bearings of a specially constructed horizontal column testing rig. A schematic plan view of a test panel in the test rig is shown in Fig. 4. The measured dimensions of the test specimens, including the initial out-of-straightness Δ_0 of the top chord relative to the outer node points, are summarised in Table 2.

Axial compression was exerted by a DARTEC 2000 kN (449 kips) capacity servo-controlled hydraulic ram which could be operated in load, stroke or extensometer control modes. Operating the DARTEC by extensometer control of the top-chord axial displacement permitted concise and stable tracking of panel behaviour right up to and beyond the ultimate load. The 2000 kN (449 kips) capacity multi-directional pinned bearings between which the top chord was located concentrically have a bearing length (l_b) of 225 mm (8.86 in.). Consequently, the panel overall length L used in all numerical calculations was equal to the specimen length ($2l_s + 2l_o$) plus twice the bearing length ($2l_b$) (Fig. 4).

An arrangement of screwed rods and end blocks allowed the use of a hand operated hydraulic jack to apply axial force to the bottom chord and consequently to apply the required curvature to the top chord. This system simulated the effect in a STRARCH building of the prestressing strand closing the bottom chord gaps.

The test procedure aimed to simulate the behaviour of the top chord in a STRARCH frame, and therefore progressed in the following two stages:

1. The top chord was curved a pre-determined amount by jacking the bottom chord nodes together and applying curvature through the web members. The level of top chord precurvature was monitored by measuring the lateral deflection of the mid-span position of the top chord and also monitoring the curvature at a strain gauge pair located near the centre of the specimen. This stage of the test procedure simulated the curvature-inducing erection procedure of the STRARCH system.
2. The bottom chord was then locked into position at a constant length and axial loading of the top chord proceeded until the ultimate load. A sufficient number of load increments was employed so as to clearly define the load-deformation characteristics and the ultimate load. The test specimens were loaded beyond the ultimate load to a load which varied from 79 % of the ultimate load for Panel SP12 to 95 % of the ultimate load for Panel SP15.

Each of the four test panels with a 102 SHS top chord (Panels SP12–SP14) was tested with a different level of precurvature, including one panel (SP12) which was almost straight. Because only one panel with a 76 SHS top chord was tested, only one level of precurvature was used for this size section.

3.3.2 Panel Test Results

The initial lateral displacements and curvatures induced by precurving the top chord prior to axial loading are given in Table 2 together with the maximum jack load attained, P_u, and the ratio of the maximum jack load to the stub column strength, P_u/P_{Su}. In Table 2, v_{10} is the initial lateral displacement at the central panel point of the top chord and κ_{10} is the initial curvature at a distance of 150 mm (5.91 in.) (for Panel SP14) or 100 mm (3.94 in.) (for Panels SP12, SP13 and SP15) from the central panel point of the top chord. The initial lateral displacement v_{20} and the initial curvature κ_{20} are both located at the mid-position of each top chord segment. The initial curvature κ_{30} is located halfway between the outer panel point and the position of κ_{20} for each top chord segment. Panels SP13–SP15 failed by in-plane bending and Panel SP12 failed by a combination of out-of-plane and in-plane deformations. For Panel SP12, out-of-plane displacements were not observed until after the ultimate load was passed and it is therefore believed that the pre-ultimate response and maximum load were not affected by the out-of-plane behaviour.

The axial load applied by the DARTEC jack, P, normalised with respect to the experimental stub column load, P_{Su}, has been plotted against axial displacement, u, of the top chord, normalised with respect to the panel overall length L, in Fig. 5 for Panels SP12–SP15. The increasing initial curvature of Panels SP12–SP14 clearly decreases the axial stiffness between pinned ends, as shown by the decreasing initial slope of the dimensionless load versus axial displacement graphs in Fig. 5. All tests exhibited ductile post-ultimate local behaviour as a consequence of the low component plate slenderness ratios (b/t) of the 102 SHS and 76 SHS top chord sections which are 18.7 and 13.6 respectively. The experimental load versus displacement curves for a typical test panel (Panel

SP13) are given in Figs 9 and 10 of the following section of the paper together with the response predicted by the nonlinear finite element analysis.

4 SIMULATION WITH FINITE ELEMENT ANALYSIS

4.1 General

The experimental behaviour of the test panels described previously is compared with the theoretical behaviour predicted by the nonlinear finite element analysis which incorporates a rigorous treatment of the geometric and material nonlinear aspects of the panel behaviour. The experimentally determined cross-section geometry, geometric imperfections, residual stress distribution, stress-strain behaviour and joint stiffness were all modelled accurately in the nonlinear analysis.

4.2 Analytical Modelling of Section and Material Properties

4.2.1 Analytical Model for Section Geometry

An accurate consideration of the spread of yielding throughout the top chord section requires a realistic representation of top chord geometry. This is achieved here by modelling the top chord as a series of straight and uniformly curved strips, similar to the description employed in finite strip analysis. Each strip can have have its own characteristic material behaviour, residual stress distribution and monitoring station layout. The top chord section model adopted here, including the monitoring station layout used for describing the current state of strain, stress and yield stress around the section is shown in Fig. 6(a). The average measured plate thicknesses of 4.76 mm (0.187 in.) for the 76 SHS and 4.75 mm (0.187 in.) for the 102 SHS, rather than the nominal thickness of 4.9 mm (0.193 in.), was used in the modelling of the top chord. The web members and bottom chord, which did not undergo yielding in the analyses, were modelled on the nominal geometry.

4.2.2 Analytical Model for Residual Stress and Material Behaviour

At any point around the perimeter of a square hollow section, the residual stress may be considered to be composed of a membrane and a through-thickness component. As described in Davison & Birkemoe (1983), the through-thickness component may furthermore be decomposed into one distribution varying linearly through the thickness, termed the bending component here, and a second distribution varying irregularly through the thickness and representing the state of residual stress in a released coupon, termed the layering component here. The analytical models for the distribution of residual stress through the thickness and around the perimeter of the 102 SHS section are shown in conjunction with the experimental results in Fig. 7.

As explained in a previous section, the stress-strain curve obtained in a tension coupon test only reflects average material behaviour through the thickness and *includes* the rounding effects of residual stress. The approach adopted in the present work was to assume that the material behaviour is represented by the stress-strain curves obtained directly in the tension coupon tests which therefore includes the bending (σ_{Rb}) and layering (σ_{Rl}) residual stress distributions, but excludes the membrane distribution (σ_{Rm}) shown in Fig. 7. Consequently, the membrane residual stress component was the only distribution incorporated into the panel test simulations described in this paper.

Tension tests, compression tests and combined tension-compression tests were performed to ascertain material behaviour. In this paper, the material behaviour is believed to be most accurately represented by the tension coupon results. The tension-compression coupons displayed the Bauschinger effect (Abel 1987) although the unloading response was close to linear at least to unloading to zero stress. The finite element analysis results indicated that the strength and behaviour of the panels could be accurately predicted without modelling the Bauschinger effect.

The stress-strain curves obtained in the tension tests, which include the rounding influence of bending and layering residual stress, have been accurately modelled using 7 linear segments, as described in Clarke & Hancock (1989). A linearised approach was found to be more accurate and convenient than fitting a continuous analytical function to the experimental stress-strain curve and also displayed advantages in terms of computational efficiency compared with a continuous function. Different models of material behaviour were assumed for the flats and corners of the 102 SHS section used as the top chord in Panels SP12–SP14. Panel SP15 comprised a 76 SHS top chord section for which no tension coupons were tested. The material stress-strain curves for Panel SP15 were therefore assumed to be identical in shape to those used for Panels SP12–SP14, but scaled uniformly by the ratio of the average 0.2% proof stress of the 76 SHS stub column to the average 0.2% proof stress of the 102 SHS stub column. This ratio was determined experimentally to be 1.15.

4.3 Simulation of the Panel Tests

4.3.1 Finite Element Model of Panel

The finite element model of the test panels, which was used to simulate the experimentally observed behaviour, is shown in Fig. 6(b). Ten equal length elements were used for each top chord segment between panel points and a nominal length of 180 mm (7.09 in.) was adopted for the top chord outstand l_o (Fig. 4). The test rig bearings were modelled by a single 'bearing' element of length 225 mm (8.86 in.) at each end of the panel. The 'bearing' elements were defined to be of essentially rigid axial and flexural stiffness. The behaviour of the bottom chord was elastic and not of prime importance and so two elements were considered sufficient to model it.

Each of the four web members were discretised into six elements, although only four equal length elements were used over most of the member length, as shown in Fig. 6(b).

The two remaining elements, termed 'joint' elements here, connected each web member to the top and bottom chords and were used to simulate the non-rigid stiffness of the web to top and bottom chord connections. The axial rigidity, EA, of the 'joint' elements was defined to be the same as for the web members, but the rotational stiffness, k_θ, of the joint obtained experimentally was modelled by a very short element of length $L = 0.1\,\text{mm}$ (0.004 in.), second moment of area I, and Young's modulus E, such that

$$k_\theta = \frac{M}{\theta} = \frac{EI}{L} = 12.5 \times 10^6\,\text{Nmm} = 9.22\,\text{kip ft} \qquad (17)$$

The formula for joint rotational stiffness given by Eqn 17 above is only valid if the element can be considered to be subject to a uniform distribution of bending moment.

If the panel geometry was defined to be perfectly symmetric about the centreline perpendicular to the top chord, then the deformations and failure mode observed would also be symmetric. Since the failure mode observed for Panels SP12–SP15 involved non-symmetric deformations, it was necessary to introduce some degree of asymmetry into the finite element model of the top chord. This was achieved by giving one segment of the top chord an initial imperfection in the shape of a sine-squared function with a maximum out-of-straightness of 1 in 10^4.

4.3.2 Simulation of the Experimental Test Procedure

An accurate theoretical simulation of the panel tests must model the two stage experimental procedure described previously. This was accomplished in the present work as follows:

1. The application of curvature to the top chord was achieved by applying increments of initial compressive membrane strain to the bottom chord elements. This is equivalent to 'shrinking' or 'cooling' the bottom chord to induce curvature in the top chord via the web members. When the required level of precurvature was achieved, the load factor on the initial strains was held constant thereafter.
2. A 'proportional' load factor was used to increment a reference top chord axial load up until and beyond the ultimate load.

In the precurving stage, there are many parameters which could be used to indicate when the simulated precurvature accurately reflected the precurvature obtained experimentally. The curvatures at various positions along the top chord profile can attempt to be matched, or lateral displacements of the top chord can be monitored. A simple and effective simulation of the precurved experimental top chord profile could be achieved if the initial central lateral deflection, v_{10}, of the simulated and experimental profiles coincided. This criterion has therefore been adopted for the theoretical analyses reported here.

During the initial straining and pre-ultimate axial loading stages, the conventional Newton-Raphson iterative strategy was employed. Convergence obtained with iterative solution

strategies based on the modified Newton-Raphson method (Clarke & Hancock 1988) was often slow or did not occur at all, most probably because the loading was non-proportional and many parts of the structure unload elastically from the yield surface throughout the axial loading stage. The ultimate load was traversed by altering the iterative strategy from conventional Newton-Raphson to the modified Newton-Raphson based displacement control (Powell & Simons 1981) just prior to maximum load. The controlled displacement was the lateral displacement v_2 of the failing segment (see Fig. 10 later). Iterative control was switched back to the conventional Newton-Raphson method to obtain the post-ultimate response.

The two stage analytical procedure and the numerical techniques described in this section facilitated an accurate simulation of the experimental behaviour. The results of the simulations and the application to the design of the top chord in stressed arch frames is discussed hereafter.

4.3.3 Results of the Finite Element Analysis

The ultimate loads and mean initial curvatures κ_{20} obtained experimentally are compared with the values obtained in the finite element analysis in Table 3. Agreement between the experimental and finite element maximum loads is excellent, with the maximum discrepancy being only 1.6 %. For a typical panel (Panel SP13), the finite element results are compared with the experimental behaviour in Figs. 8 to 10. The experimental load versus axial displacement (u) response for Panel SP13 is compared with the finite element prediction in Fig. 8. Figures 9 and 10 display the corresponding comparison for the lateral displacement v_1 at the central node of the top chord, and the lateral displacements v_2 at the mid-position of each top chord segment. The axial load P represents the load applied by the jack in the experimental procedure and has been normalised with respect to the experimental stub column ultimate load, P_{Su}. The displacements u, v_1 and v_2 are normalised with respect to the panel overall length, L. Good agreement between the theoretical and experimental results is evident in Figs 8, 9 and 10. Similar comparisons for Panels SP12, SP14 and SP15 shown in Clarke & Hancock (1989) also display good agreement.

4.4 Application of the Panel Test Results to the Design of the Top Chord in Stressed Arch Frames

The stressed arch structural system concept is a unique development in steel structures for which existing steel design standards are not written to provide a simple and economical design of the top chord. The complexity of the design problem arises because the structural behaviour of the top chord in the initial curving (erection) stage differs markedly from its behaviour under downwards live load such as snow load. To simply superpose the stresses or stress resultants arising from the two stages of behaviour will most likely lead to an uneconomical design.

The experimental results of panel strength described in this paper can be used as the basis of a rational design procedure for the top chord of stressed arch frames. Assuming

that the sections used for the top chord have a sufficiently low plate slenderness so that local buckling effects can be disregarded, the strength of the top chord is likely to be a function of the level of initial curvature and the overall slenderness between panel points, l_s/r. Theoretical graphs of maximum applied axial load versus initial curvature are shown in Fig. 11 where the results of the four panel tests have been plotted for comparison. The initial curvature used is the mean initial curvature, κ_{20}, at the mid-position of each panel segment. In the figure the axial load has been non-dimensionalised with respect to the experimental stub column strength P_{Su}, and the initial curvature has been non-dimensionalised with respect to the nominal curvature at first yield, κ_{Yn}, calculated using engineering bending theory and a yield stress of 350 MPa (51 ksi). Experimental and theoretical agreement is good, although a notable discrepancy in the initial curvature is apparent for the most highly curved panel (SP14), despite the fact that the initial central lateral deflections of this panel coincided. It is observed that the finite element solution for Panel SP12 lies slightly above the solid line in Fig. 11. The explanation for this is that Panel SP12 was subject to an initial loading-unloading cycle before initial straining which was accounted for in the finite element simulation and had the effect of raising the ultimate load marginally.

The fact that satisfactory agreement was achieved between the theoretical and experimental results indicates that the finite element analysis is a valuable tool for developing design data for the top chord of stressed arch frames. The results in Fig. 11 are likely to be conservative estimates of the top chord strength in stressed arch frames. This is because the pin-ended support conditions and the presence of the top chord outstand (l_o) and bearing length (l_b) in the test panels are all weakening effects compared to the continuous nature of the top chord in a complete frame. Further economies in design are therefore possible by applying the finite element analysis to study the behaviour of pin-ended panels which have the axial force applied at the web to top chord connection, or furthermore, to the analysis of complete frames including simulation of the erection procedure.

5 CONCLUSIONS

The paper has described a geometric and material nonlinear finite element analysis suited to the full range collapse analysis of columns, beam-columns, arches and plane frames in which cross-section distortion does not occur prior to attainment of ultimate load. An experimental investigation into the strength of sub-assemblages of stressed arch frames has also been presented. The purpose of the tests was to determine the effect of erection curvature on the compressive strength of the top chord and to determine its nonlinear behaviour.

The experimental results have been accurately simulated using the finite element analysis, with the maximum discrepancy in the ultimate load for the four panels simulated being only 1.6 %. The simulations incorporated rigorous modelling of the initial top chord curving procedure, the measured geometric imperfections, cross-section geometry and the variation in stress-strain behaviour and residual stress around the cross-section perimeter. Theoretical graphs of maximum load versus initial curvature have been prepared for two top chord section sizes.

The finite element analysis program has therefore been shown to be a valuable tool for studying the nonlinear behaviour of sub-assemblages of stressed arch frames and for the development of design data for the top chord. The potential for applying the program to the analysis of complete frames is consequently most encouraging.

6 ACKNOWLEDGEMENTS

This paper forms part of a research program into the behaviour of steel structures undertaken in the Centre for Advanced Structural Engineering, within the School of Civil and Mining Engineering at the University of Sydney.

The authors are grateful to Strarch International Limited for providing the specimens and funding for the test program, and for permission to publish the results. Numerical computations were performed on an IBM PS/2 Model 70 microcomputer purchased with funds provided by Strarch International Limited. The contribution of Dr Peter Key, Senior Research Engineer, Strarch International Limited, to the test program is much appreciated.

The first author was supported by a Commonwealth Postgraduate Research Award provided by the Australian Government and a supplementary grant provided by Strarch International Limited through the Civil and Mining Engineering Foundation at the University of Sydney.

7 APPENDIX I. REFERENCES

[1] Abel, A. (1987) "Historical Perspectives and some of the Main Features of the Bauschinger Effect", *Materials Forum*, Vol. 10, No. 1, pp. 11–26.

[2] Armen, H. (1979) "Assumptions, Models, and Computational Methods for Plasticity", *Computers and Structures*, Vol. 10, pp. 161–174.

[3] Beck, V. R. and Lay, M. G. (1972) "Structural Tests on Cold-Rolled Hollow Sections", *Report S5/18*, Melbourne Research Laboratories, Australia.

[4] Clarke, M. J. and Hancock, G. J. (1988) "A Study of Incremental-Iterative Strategies for Nonlinear Analyses", *Research Report*, No. R587, School of Civil and Mining Engineering, University of Sydney, December (also accepted for publication in *International Journal for Numerical Methods in Engineering*).

[5] Clarke, M. J. and Hancock, G. J. (1989) "A Finite Element Nonlinear Analysis of Stressed Arch Frames", *Research Report,* No. R605, School of Civil and Mining Engineering, University of Sydney, December.

[6] Cook, R. D. (1981) *Concepts and Applications of Finite Element Analysis*, 2nd edn, Wiley and Sons, New York.

[7] Crisfield, M. A. (1981) "A Fast Incremental/Iterative Solution Procedure that Handles "Snap-through" ", *Computers and Structures*, Vol. 13, pp. 55–62.

[8] Davison, T. A. and Birkemoe, P. C. (1983) "Column Behaviour of Cold-Formed Hollow Structural Steel Shapes", *Canadian Journal of Civil Engineering*, Vol. 10, No. 1, pp. 125–141.

[9] Engineering News-Record (1988) "Cabled Truss Curves as it Rises", *Engineering News-Record,* Vol. 221, No. 15, October 13, pp. 14–15.

[10] Hancock, G. J., Key, P. W. and Olsen, C. J. (1988) "Structural Behaviour of a Stressed Arch Structural System", *Recent Developments in Cold-Formed Steel Design and Construction,* Ninth International Specialty Conference on Cold-Formed Steel Structures, November 8–9, University of Missouri–Rolla, St. Louis, Missouri.

[11] Hancock, G. J., Key, P. W., Clarke, M. J. and Olsen C. J. (1989) "Structural Tests on the Top Chord of Strarch (Stressed Arch) Frames", *Proceedings,* Pacific Structural Steel Conference, Gold Coast, Queensland, Australia, Australian Institute of Steel Construction.

[12] Karren K. W. (1967) "Corner Properties of Cold-Formed Steel Shapes", *Journal of the Structural Division,* ASCE, Vol. 93, No. ST1, pp. 401–432.

[13] Kato, B. (1982) "Cold Formed Welded Steel Tubular Members", Chapter 5 of *Axially Compressed Structures*, Applied Science.

[14] Key, P. W. and Hancock, G. J. (1988) "A Theoretical Investigation of the Column Behaviour of Cold-Formed Square Hollow Sections", *Research Report*, No. R584, School of Civil and Mining Engineering, University of Sydney, Australia, December.

[15] Key, P. W., Hasan, S. W. and Hancock, G. J. (1988) "Column Behaviour of Cold-Formed Hollow Sections", *Journal of Structural Engineering*, ASCE, Vol. 114, No. 2, pp. 390–407.

[16] Mendelson, A. (1968) *Plasticity: Theory and Application*, Macmillan, New York.

[17] Nyssen, C. (1981) "An Efficient and Accurate Iterative Method, Allowing Large Incremental Steps, to Solve Elasto-Plastic Problems", *Computers and Structures,* Vol. 13, pp. 63–71.

[18] Powell, G. and Simons, J. (1981) "Improved Iteration Strategy for Nonlinear Structures", *International Journal for Numerical Methods in Engineering*, Vol. 17, pp. 1455–1467.

[19] Riks, E. (1979) "An Incremental Approach to the Solution of Snapping and Buckling Problems", *International Journal of Solids and Structures,* Vol. 15, pp. 529–551.

[20] Rotter, J. M. and Jumikis, P. T. (1988) "Nonlinear Strain-Displacement Relations for Axisymmetric Thin Shells", *Research Report*, No. R563, School of Civil and Mining Engineering, University of Sydney, February.

[21] Standards Association of Australia (1981) *Structural Steel Hollow Sections,* AS1163, SAA, Sydney, Australia.

[22] Teng, J. G. and Rotter, J. M. (1989) "Elastic-Plastic Large Deflection Analysis of Axisymmetric Shells", *Computers and Structures*, Vol. 31, No. 2, pp. 211–233.

[23] University of Sydney (1987a) "Strarch Panel Tests to Determine Top Chord Strength", *Investigation Report,* No. S621, School of Civil and Mining Engineering, University of Sydney, September.

[24] University of Sydney (1987b) "Strarch Panel Test SP11", *Test Record,* No. T447, School of Civil and Mining Engineering, University of Sydney, October.

[25] University of Sydney (1989) "Strarch Panel Tests SP12–SP15", *Investigation Report,* No. S697, School of Civil and Mining Engineering, University of Sydney, January.

[26] Zienkiewicz, O. C. (1977) *The Finite Element Method*, 3rd edn, McGraw-Hill, New York.

8 APPENDIX II. NOTATION

The following symbols are used in this paper:

$\{d_e\}$	Vector of element nodal displacements
$[D_T]$	Tangent modulus matrix for cross-section
e_{un}	Percentage uniform elongation to ultimate strength
E	Young's modulus
E_t	Tangent modulus to stress-strain curve
F_Y	Yield stress
$[k_T]$	Element tangent stiffness matrix
k_θ	Joint rotational stiffness
l_b	Bearing length in test rig
l_o	Length of top chord outstand
l_s	Length of top chord segment between panel points
L	Overall length of test panel; element half-length
N_s	Membrane stress resultant of axial force
M_s	Bending stress resultant of bending moment
P	Axial load exerted by jack
P_u	Experimental panel maximum load
P_{Su}	Experimental stub column maximum load
r	Radius of gyration of cross-section
s	Arc-length coordinate along element
$\{S\}$	Vector of generalised stress resultants
u	Generalised axial displacement
v	Generalised lateral displacement
u, v	Displacements in global cartesian coordinates
$\bar{u}, \bar{v}$	Displacements in local curvilinear coordinates
x, y	Global coordinate axes

β_1, β_2	Pseudo-rotations in strain-displacement relations
Δ_0	Maximum out-of-straightness of panel
ϵ_s^z	Longitudinal strain at level z above element reference line
ϵ_s, κ_s	Membrane strain and curvature at element reference line
ϵ_{so}, κ_{so}	Initial membrane strain and initial curvature at element reference line
$\{\varepsilon\}$	Vector of generalised strains
$\{\varepsilon_o\}$	Vector of generalised initial strains
κ	Curvature
κ_{Yn}	Nominal curvature at first yield
σ_s	Longitudinal stress at a point
σ_u	Ultimate tensile strength
ϕ	Angle defining element geometry
$\{\phi\}$	Vector of element nodal loads

Table 1. Mean results of coupon tests for 102 SHS

Coupon type	Location	Tension					Compression		
		$\sigma_{0.2}$ (MPa)	$\sigma_{1.0}$ (MPa)	σ_u (MPa)	e_{un} %	$\sigma_u/\sigma_{0.2}$	$\sigma_{0.2}$ (MPa)	$\sigma_{0.5}$ (MPa)	$\sigma_{1.0}$ (MPa)
Tension	Corner	469	504	504	1.74	1.07	—	—	—
Tension	Flat	349	372	414	21.7	1.19	—	—	—
Compression	Flat	—	—	—	—	—	−323	−353	−365
Tens.–comp.	Corner	460	—	—	—	—	−440	−488	—
Tens.–comp.	Flat	349	—	—	—	—	−284	−338	—

1 ksi = 6.895 MPa

Table 2. Panel dimensions, initial displacements, initial curvatures and test results

Panel	SP12	SP13	SP14	SP15
Panel dimensions*				
Top chord size (mm)	102 SHS	102 SHS	102 SHS	76 SHS
Δ_0 (mm)	3.0	3.0	3.0	9.5
l_s (mm)	1800	1800	1800	1800
l_o (mm)	179	177	180	176
h (mm)	2460	2460	2460	2460
Slenderness l_s/r	46.2	46.2	46.2	62.9
Initial displacements				
v_{10} (mm)	13.04	55.03	98.80	81.29
v_{20}† (mm)	3.33	13.54	26.10	19.60
Initial curvatures				
κ_{10} (10^{-6} mm^{-1})	8.18	38.17	72.36	56.47
κ_{20}† (10^{-6} mm^{-1})	4.53	16.31	26.32	24.47
κ_{30}† (10^{-6} mm^{-1})	2.53	7.88	—	12.26
Test results				
P_u (kN)	483.4	370.9	323.2	201.7
P_u/P_{Su}	0.659	0.506	0.441	0.315

* See Fig. 4 for definition of symbols

† Average of both panel segments

1 in. = 25.4 mm, 1 ft^{-1} = 3281 × 10^{-6} mm^{-1}, 1 kip = 4.45 kN

Table 3. Experimental and finite element initial curvatures and maximum loads

Panel	Initial curvature (10^{-6} mm^{-1})		Maximum load (kN)		
	Experimental $(\kappa_{20})_P$	Finite element $(\kappa_{20})_{FE}$	Experimental P_u	Finite element P_{FE}	$\frac{(P_{FE}-P_u)}{P_u}$ %
SP12	4.53	4.51	483.4	476.6	−1.4 %
SP13	16.31	16.66	370.9	373.2	+0.6 %
SP14	26.32	23.04	323.2	318.0	−1.6 %
SP15	24.47	25.24	201.7	199.2	−1.2 %

1 ft^{-1} = 3281 × 10^{-6} mm^{-1}, 1 kip = 4.45 kN

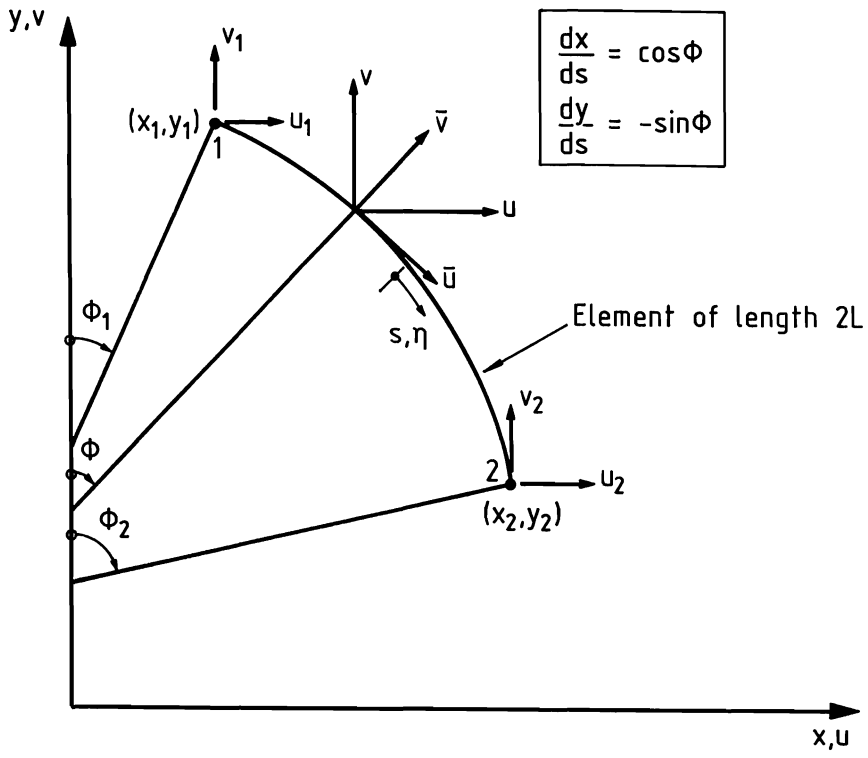

FIG.1 GEOMETRY AND LOCAL AND GLOBAL DISPLACEMENT FIELDS OF THE ELEMENT

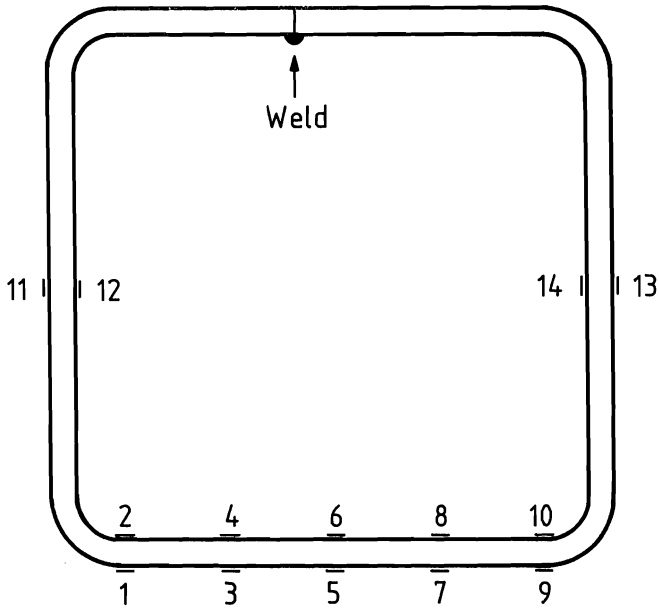

FIG.2 LOCATION OF STRAIN GAUGES FOR RESIDUAL STRESS MEASUREMENTS

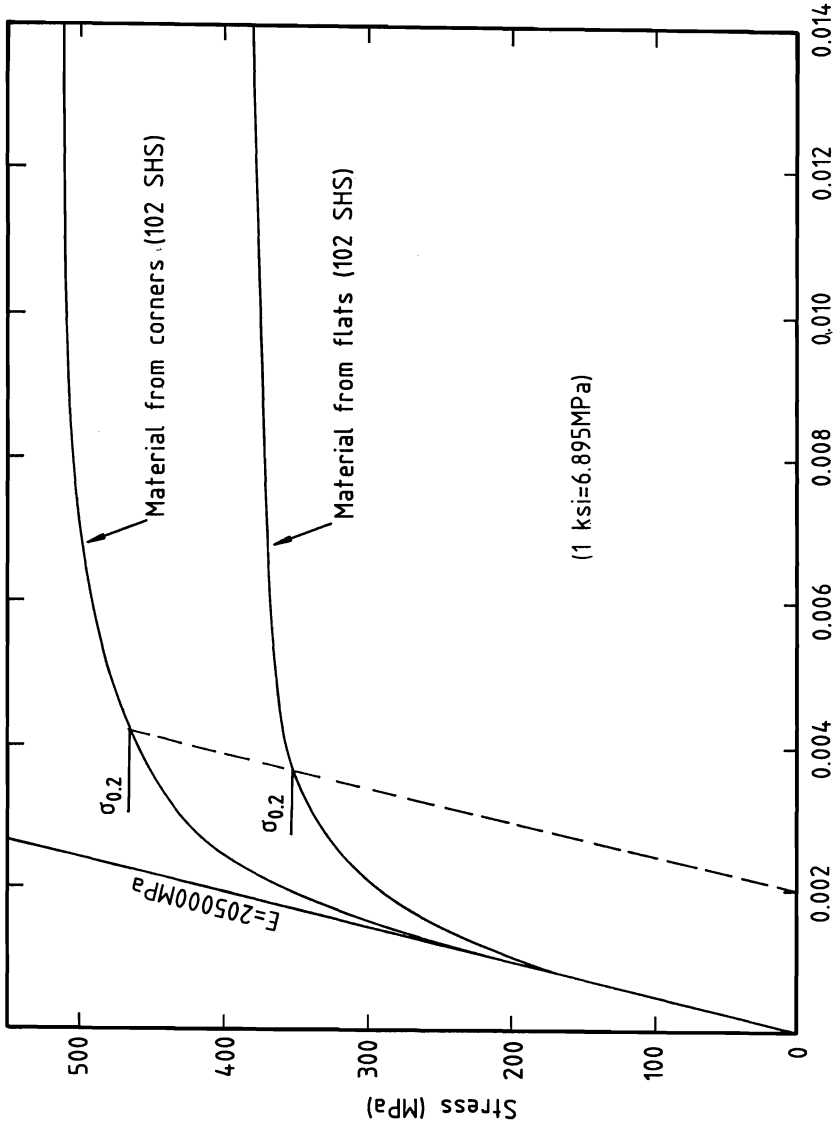

FIG.3 MEAN EXPERIMENTAL TENSION STRESS-STRAIN CURVES FOR 102 SHS

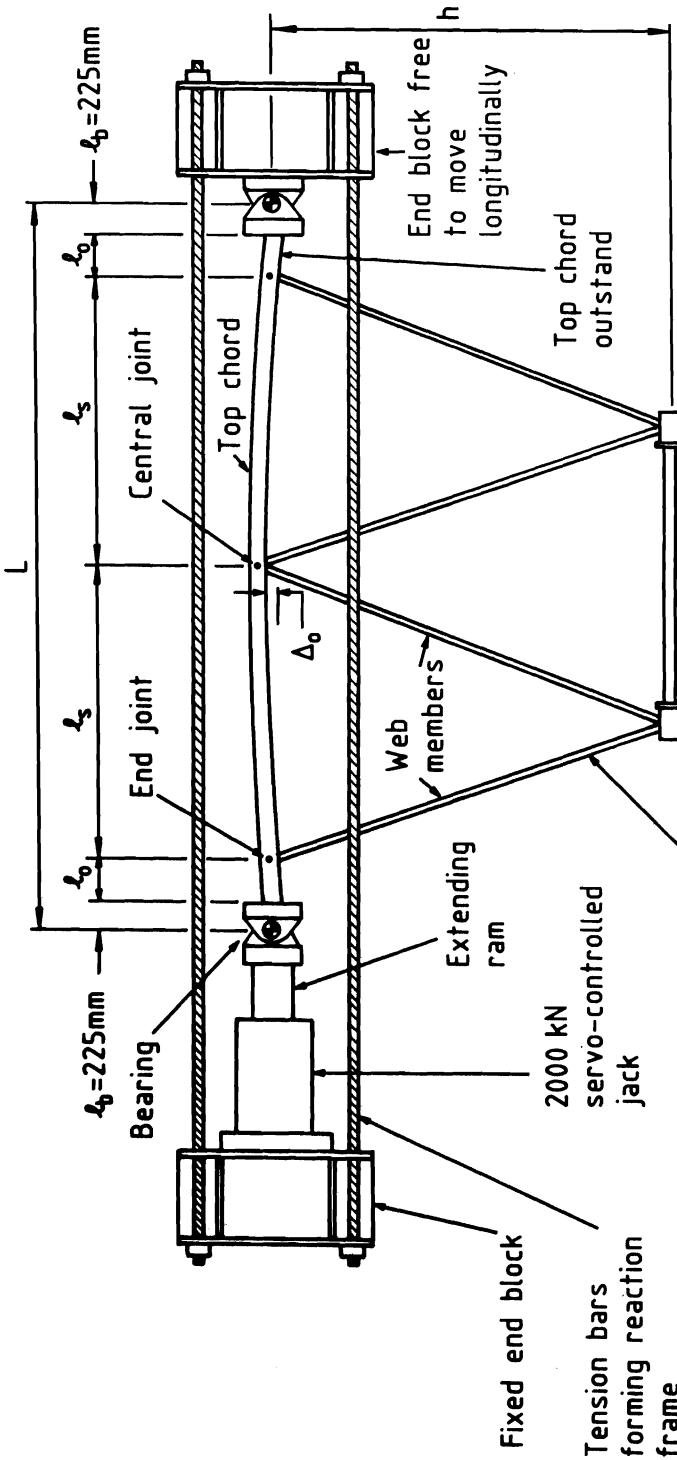

Note: The dimensions Δ_o, ℓ_s, ℓ_o and h are defined in Table 2

FIG.4 SCHEMATIC PLAN VIEW OF TEST PANEL IN TEST RIG

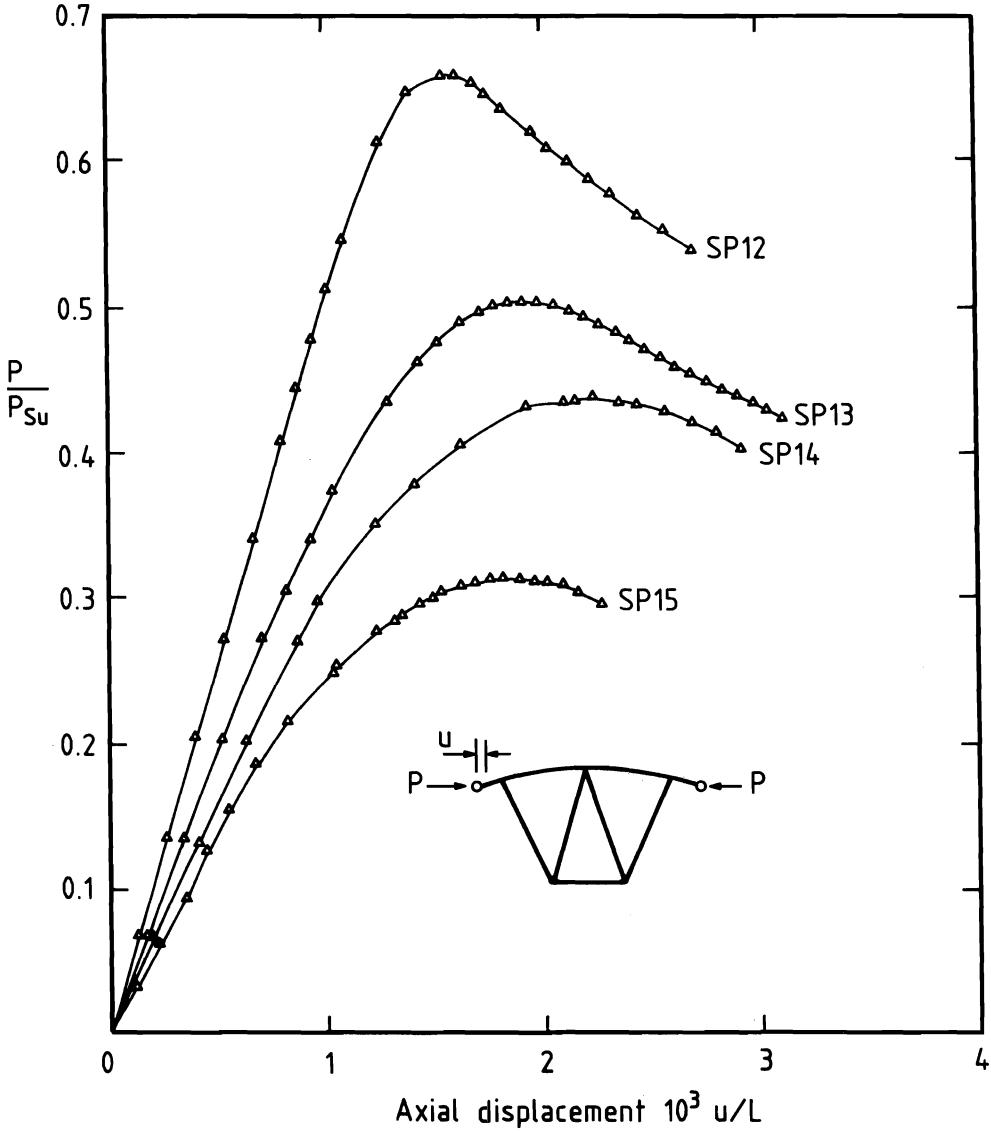

FIG.5 EXPERIMENTAL LOAD VERSUS AXIAL DISPLACEMENT FOR PANELS SP12 - SP15

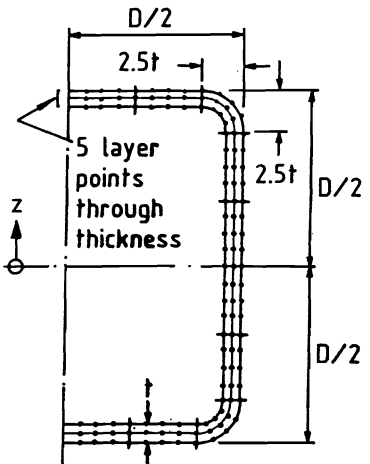

(a) Strip subdivision and monitoring point layout for top chord

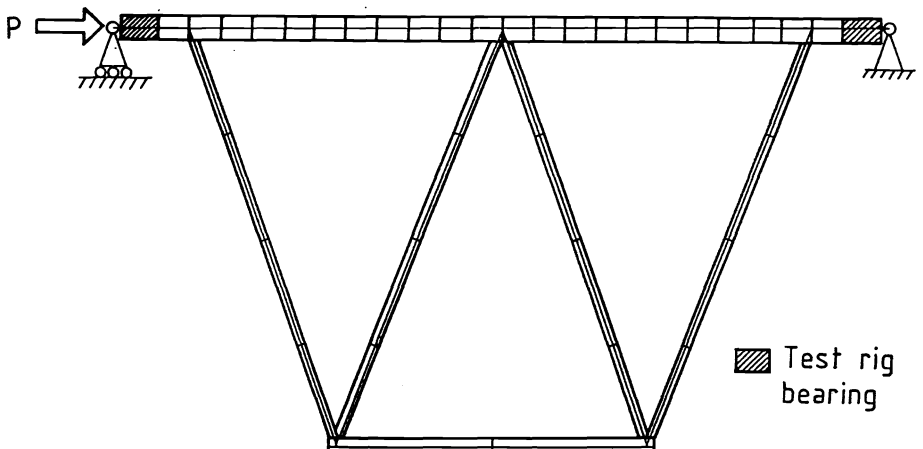

(b) Finite element model

FIG.6 TOP CHORD CROSS-SECTION DISCRETISATION AND FINITE ELEMENT MODEL OF PANEL

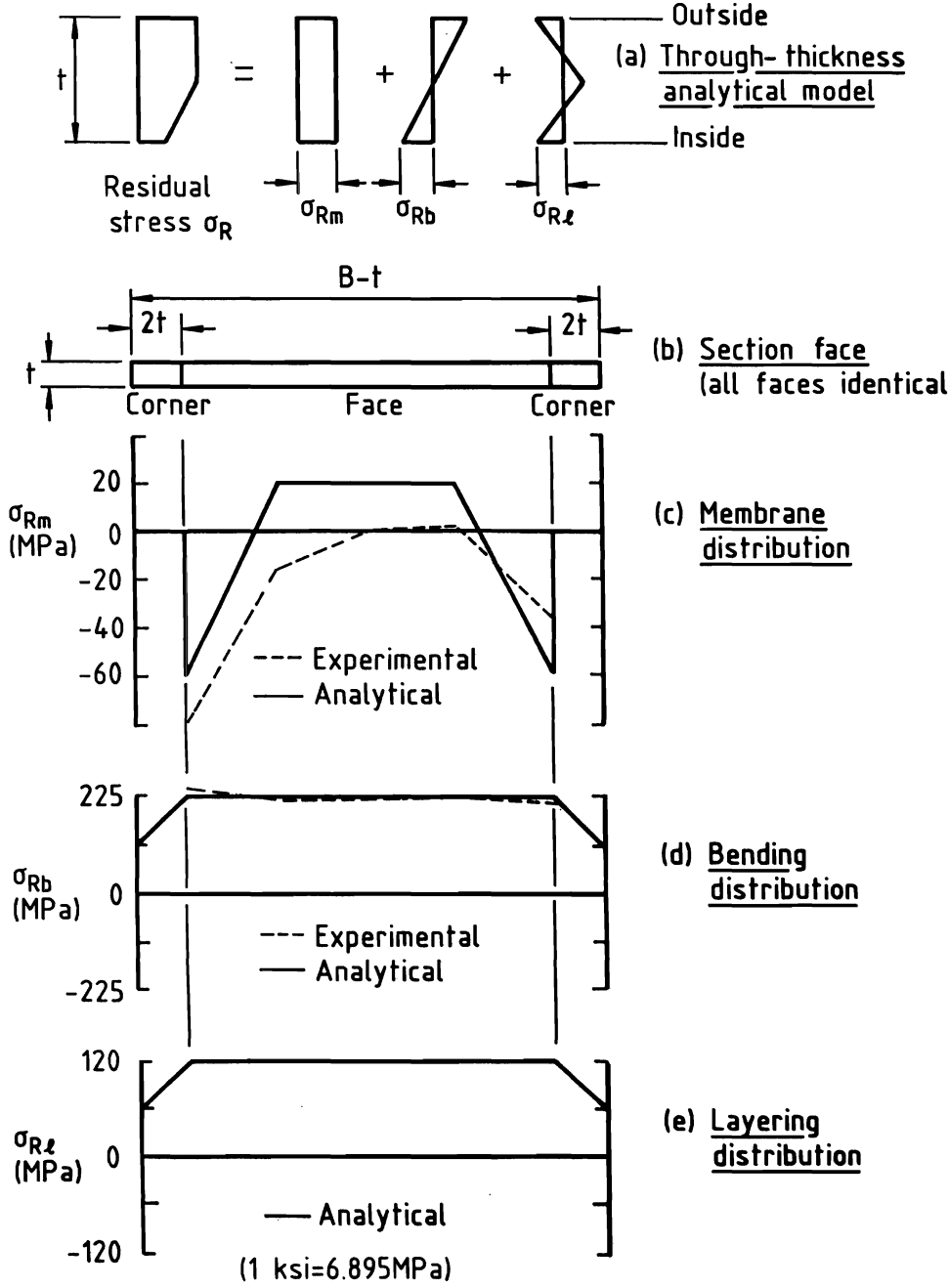

FIG.7 EXPERIMENTAL DISTRIBUTION AND ANALYTICAL MODELS FOR LONGITUDINAL RESIDUAL STRESS

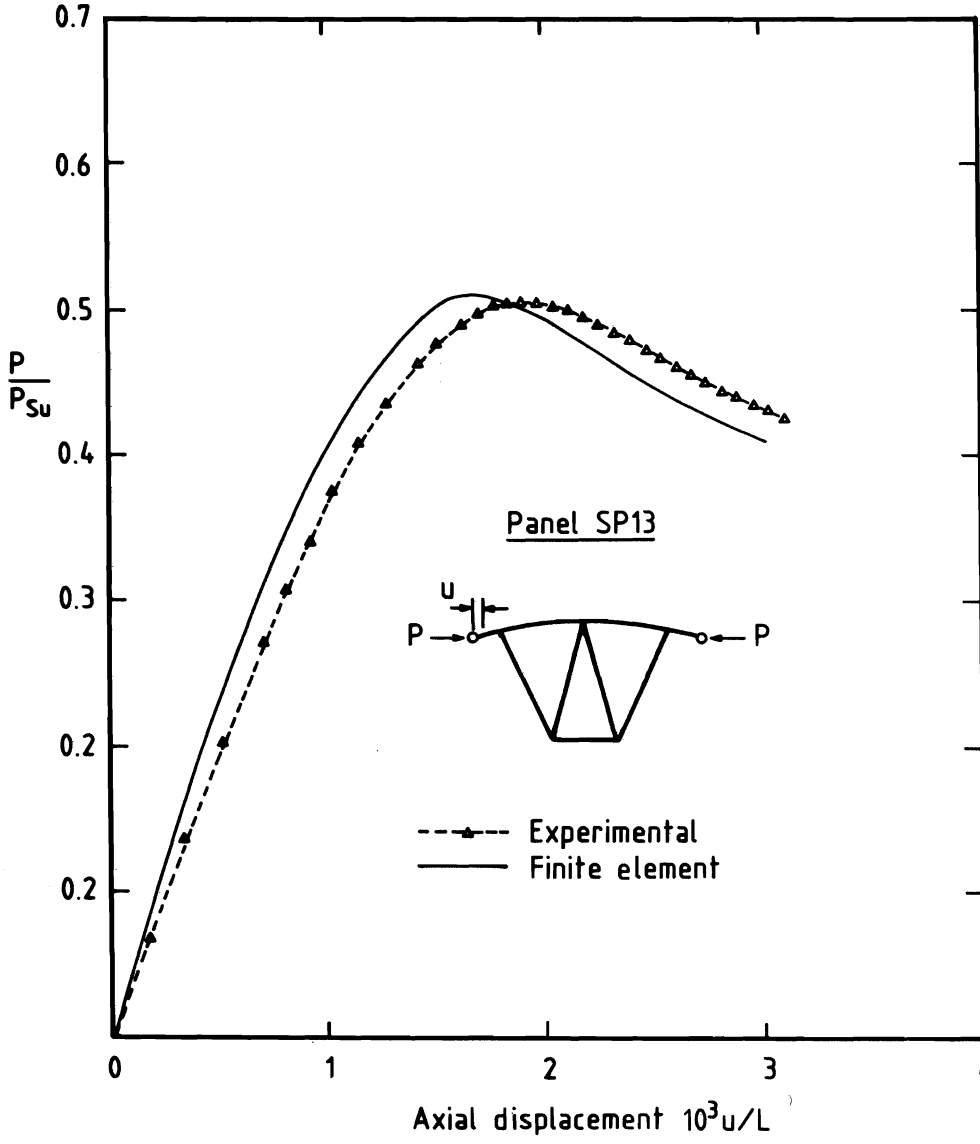

FIG.8 LOAD VERSUS AXIAL DISPLACEMENT FOR PANEL SP13

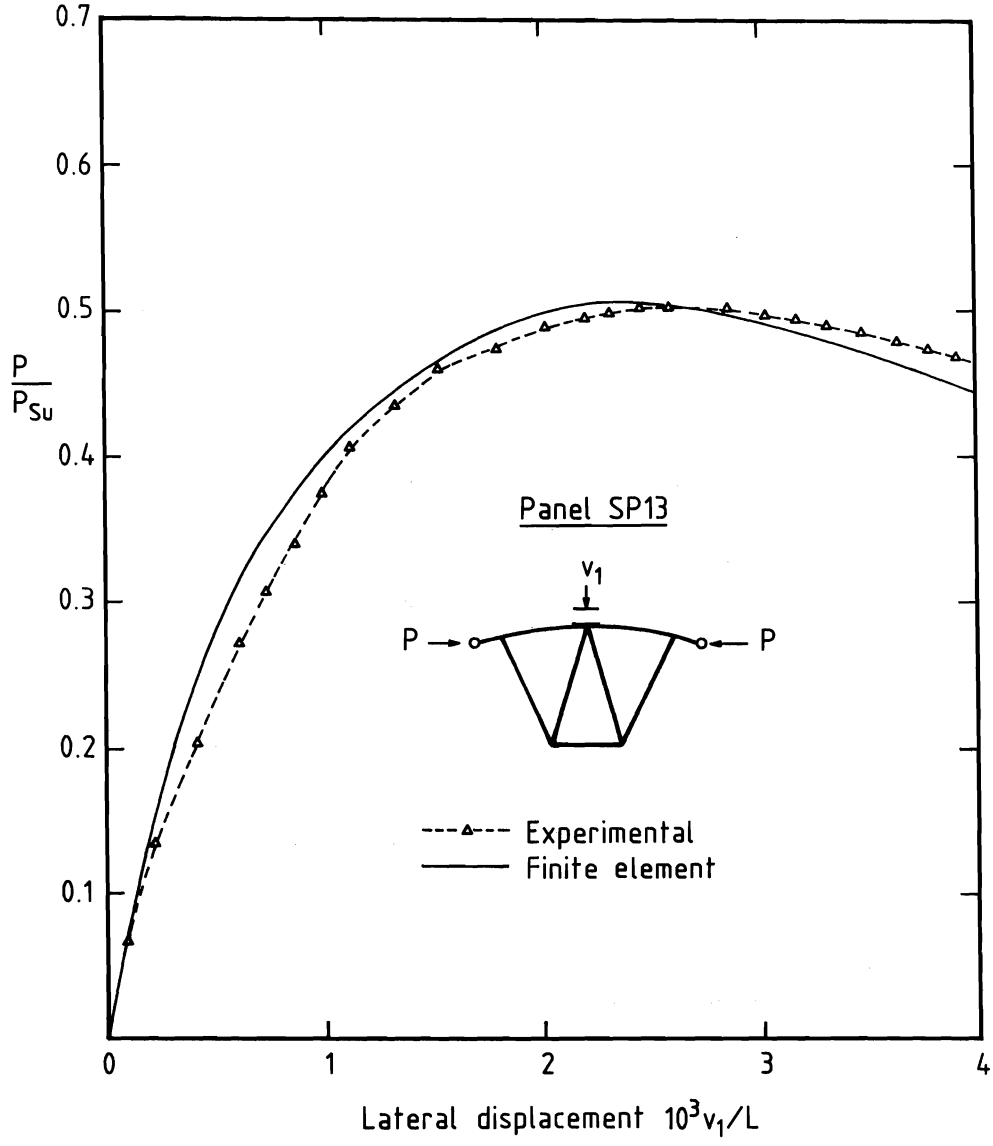

FIG.9 LOAD VERSUS LATERAL DISPLACEMENT v_1 FOR PANEL SP13

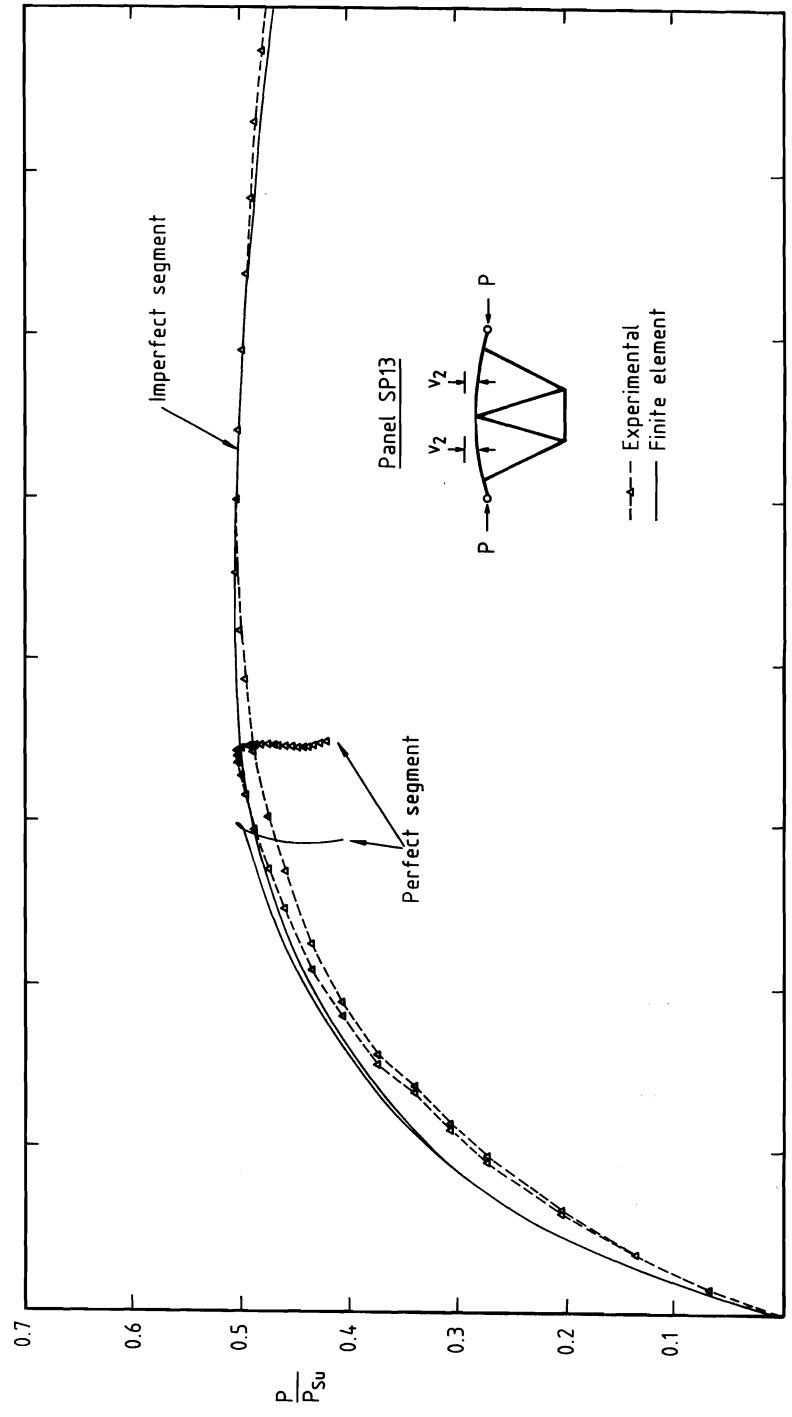

FIG.10 LOAD VERSUS LATERAL DISPLACEMENTS v_2 FOR PANEL SP13

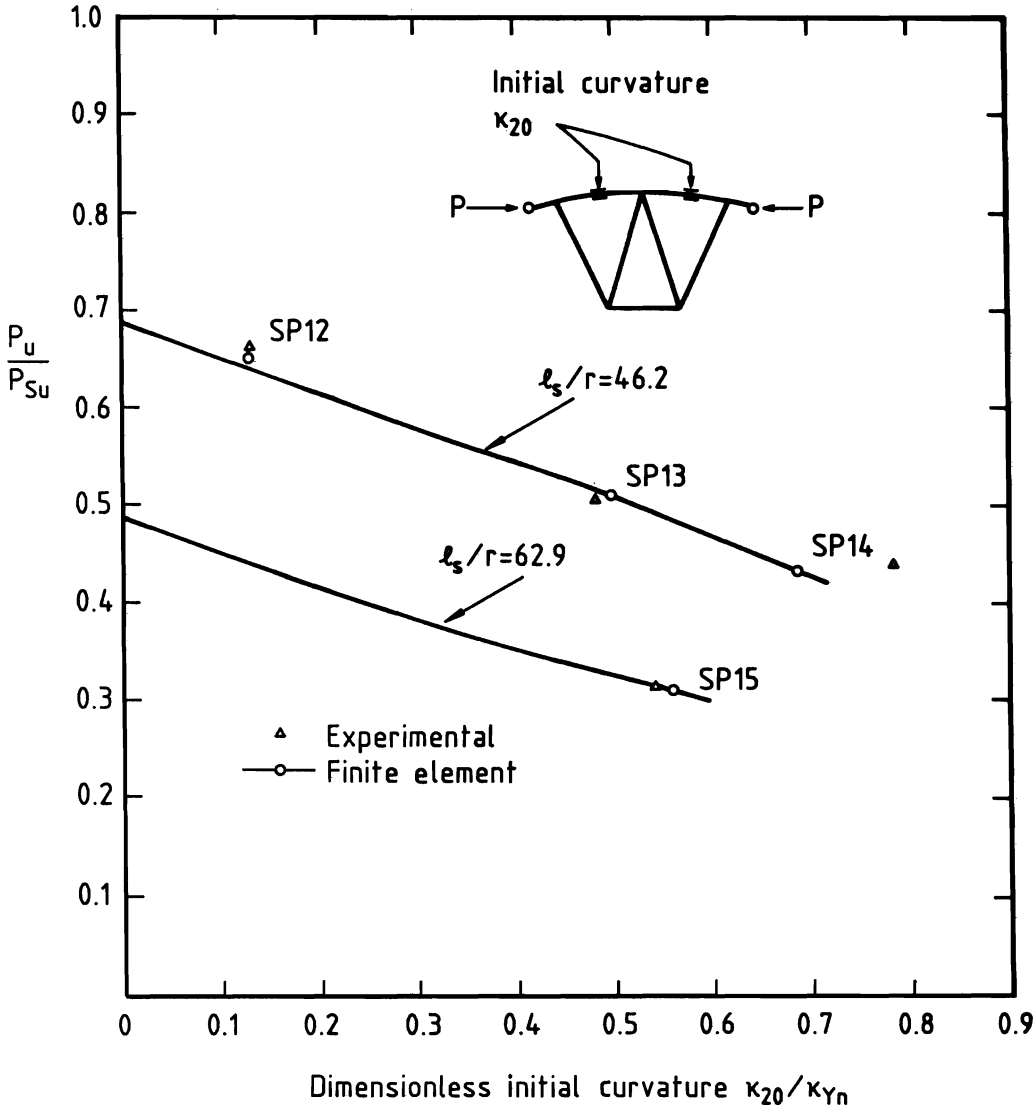

FIG.11 MAXIMUM APPLIED AXIAL LOAD VERSUS INITIAL CURVATURE κ_{20}